JACS
JOURNAL OF THE AMERICAN CHEMICAL SOCIETY
pubs.acs.org/JACS
Article

Photocatalytic C−C Coupling from Carbon Dioxide Reduction on Copper Oxide with Mixed-Valence Copper(I)/Copper(II)

Wei Wang, Chaoyuan Deng, Shijie Xie, Yangfan Li, Wanyi Zhang, Hua Sheng,* Chuncheng Chen, and Jincai Zhao

Cite This: J. Am. Chem. Soc. 2021, 143, 2984−2993
Read Online
ACCESS | Metrics & More | Article Recommendations | Supporting Information

ABSTRACT: To realize the evolution of C_{2+} hydrocarbons like C_2H_4 from CO_2 reduction in photocatalytic systems remains a great challenge, owing to the gap between the relatively lower efficiency of multielectron transfer in photocatalysis and the sluggish kinetics of C−C coupling. Herein, with Cu-doped zeolitic imidazolate framework-8 (ZIF-8) as a precursor, a hybrid photocatalyst (CuO_X@p-ZnO) with CuO_X uniformly dispersed among polycrystalline ZnO was synthesized. Upon illumination, the catalyst exhibited the ability to reduce CO_2 to C_2H_4 with a 32.9% selectivity, and the evolution rate was 2.7 $\mu mol \cdot g^{-1} \cdot h^{-1}$ with water as a hole scavenger and as high as 22.3 $\mu mol \cdot g^{-1} \cdot h^{-1}$ in the presence of triethylamine as a sacrificial agent, all of which have rarely been achieved in photocatalytic systems. The X-ray absorption fine structure spectra coupled with in situ FT-IR studies reveal that, in the original catalyst, Cu mainly existed in the form of CuO, while a unique Cu^+ surface layer upon the CuO matrix was formed during the photocatalytic reaction, and this surface Cu^+ site is the active site to anchor the in situ generated CO and further perform C−C coupling to form C_2H_4. The C−C coupling intermediate *OC−COH was experimentally identified by in situ FT-IR studies for the first time during photocatalytic CO_2 reduction. Moreover, theoretical calculations further showed the critical role of such Cu^+ sites in strengthening the binding of *CO and stabilizing the C−C coupling intermediate. This work uncovers a new paradigm to achieve the reduction of CO_2 to C_{2+} hydrocarbons in a photocatalytic system.

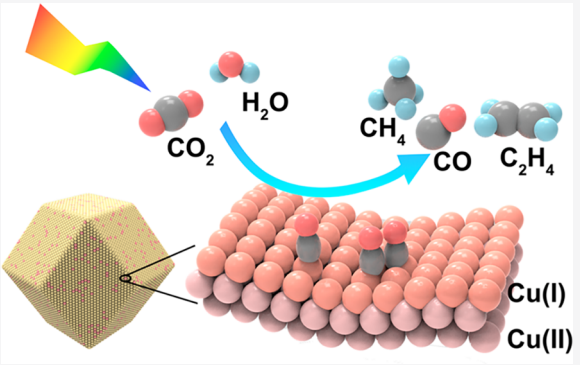

INTRODUCTION

Artificial photosynthesis has raised significant current interest due to its potential application in converting the greenhouse gas CO_2 to fuels or industrial feedstocks with solar energy as the driving force.[1] Currently, the products of light-driven CO_2 reduction are mainly limited to two-electron-reduced CO,[2,3] while the generation of further reduced hydrocarbons such as methane[4,5] or methanol[6] are also reported. Among all the possible CO_2 reduction products, the C−C coupling products, such as ethylene, that are formed via the sluggish multielectron reduction and C−C bond formation have been regarded as the most promising ones, possessing both high energy densities and market prices.[7,8] However, the efficient generation of C−C coupling products such as ethylene has rarely been achieved in photocatalytic CO_2 reduction systems.[9,10]

In the electrochemical reduction of CO_2, Cu-based catalysts have been recognized as the only metal catalysts to reduce CO_2 into C_{2+} hydrocarbons.[11−13] Moreover, recent studies have indicated that through the modulation of the oxidation states and morphologies, the generation of ethylene on Cu-based catalysts with considerable selectivity (60%−80% Faradaic efficiency) can be achieved.[12,13] However, the utilization of Cu as a cocatalyst in photocatalytic systems has rarely exhibited a similar function to form C_{2+} hydrocarbons as that in electrochemical systems.[14−16] This difference likely originates from the distinct reaction driving forces between photocatalysis and electrocatalysis: in the former, electrons with adequate capability to reduce CO_2 are provided by semiconductor catalysts excited under illumination, with far smaller densities of transferred electrons than from the latter under bias voltage.[17−19] In the generally proposed pathway for generation of the C_{2+} products (Scheme 1), CO_2 is first deoxygenated to *CO (* indicates the adsorbed intermediates or products), and then two *CO molecules on the neighboring catalytic sites are coupling, forming the key intermediate *OC−CO or its protonated form *OC−COH, with the subsequent sequential multielectron and -proton transfer completing the CO_2 reduction to generate C_{2+} products such as ethylene, ethane, or ethanol.[20−24] In the photocatalytic

Received: January 7, 2021
Published: February 11, 2021

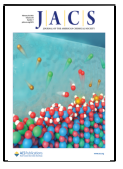

https://dx.doi.org/10.1021/jacs.1c00206
J. Am. Chem. Soc. 2021, 143, 2984−2993

Scheme 1. Generally Proposed Pathway for CO_2 Reduction to CO, CH_4, and C_2H_4

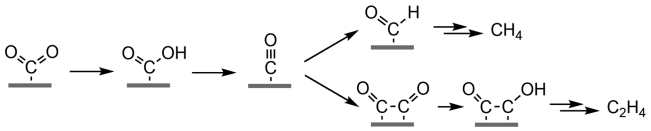

system, even in the presence of a Cu cocatalyst that should thermodynamically favor C−C coupling, the slower electron transfer rate together with the sluggish kinetics for C−C bond formation may lead to the release of *CO from the surface before it can accept the subsequent electrons to be further reduced to C_{2+} products.[9] Therefore, the success in producing C_{2+} hydrocarbon in a photocatalytic system remains a significant challenge to date, and the search for strategies to bridge the gap between the lower efficiency of multielectron transfer and sluggish kinetics for *CO coupling is still underway.

Recently, the oxidation state of Cu has been proposed to significantly affect the product selectivity in electrochemical CO_2 reduction.[24−27] The oxide-derived Cu catalyst, which is prepared by the reduction of thermally oxidized Cu, displays both improved Faradaic efficiency and reduced overpotential for C_{2+} products generation, compared with the ordinary Cu^0 catalyst. It has been proposed that the residual Cu^+ in the oxide-derived Cu catalyst plays a critical role in both strengthening the binding of *CO to the catalytic site and stabilizing the C−C coupling intermediate *OC−CO.[27] On the basis of the above propositions, the effect of the oxidation state of Cu should be even more crucial in photocatalytic CO_2 reduction than in the electrochemical procedures, as the less efficient electron transfer in the photocatalytic system requires a longer residence time of *CO on the catalytic sites to accept the subsequent electrons. Moreover, oxidized Cu^+ sites can be more stable under the reducing condition of photocatalysis than that of electrochemical procedures. In electrochemical CO_2 reduction, the electrons are transferred from the electrode to the Cu catalyst and then to the surface adsorbed CO_2, so the applied negative bias potential leads to the fast reductive depletion of most of the residual Cu^+ to Cu^0 in oxide-derived Cu catalysts before the CO_2 reduction is initiated. By contrast, in photocatalysis, the reduction of Cu^+ sites or surface adsorbed CO_2 is both driven by the electron transfer from the external semiconductor photosensitizers, so there is a competition between Cu^+ reduction and CO_2 reduction. Also considering the relatively smaller amounts of electrons transferred at a time in photocatalysis, it is very possible that the electrons mainly contribute to the surface CO_2 reduction before reducing the surface Cu^+ sites to Cu^0. Therefore, tuning the oxidation state of the Cu cocatalyst would potentially be a feasible strategy to achieve the multielectron reduction of CO_2 to C_{2+} hydrocarbons in a photocatalytic system, which, however, has never been systematically explored before.

Herein, we developed a CuO_X@p-ZnO hybrid catalyst with Cu-doped zeolitic imidazolate framework-8 (ZIF-8) as precursor, in which the initial state of copper was mainly the oxidized form of CuO, and the polycrystalline ZnO (p-ZnO) was utilized as semiconductor sensitizer to absorb light and provide electrons while the copper oxide was the catalytic center for CO_2 reduction. The CO_2 reduction products on this hybrid photocatalyst are not only limited to CO and CH_4, the C−C coupling products of C_2H_4 were also generated with 32.9% selectivity. In comparison, pristine p-ZnO without Cu showed no CO_2 reduction activity beyond CO. The combined mechanistic studies by X-ray absorption fine structure spectra (XAFS), in situ FT-IR spectra and theoretical calculations revealed that the Cu^{2+} sites in the surface layer of the CuO_X@p-ZnO catalyst were first reduced to Cu^+ in the initial stage and then being stabilized during the subsequent photocatalytic CO_2 reduction. Such specific surface Cu^+ sites on the CuO matrix were active for CO_2 reduction to C_2H_4, which tightly bound the in situ generated CO and stabilized the *OC−COH intermediate, realizing the efficient C−C coupling. This result sheds light on the significance of tuning the oxidation state of Cu and provides strategies for the generation of C_{2+} products with high selectivity in photocatalytic systems.

EXPERIMENTAL SECTION

Chemicals. Zinc acetate dihydrate (99%), methanol (≥99.9%), 2-methylimidazole (98%), copper nitrate (98%), and triethylamine (TEA) (99%) were purchased from Sigma-Aldrich. Carbon dioxide (≥99.999%) and argon gas (≥99.999%) were purchased from Beijing Zhongke Tailong Electronic Technology Co., Ltd. $^{13}CO_2$ (^{13}C, 99%; ^{18}O, <2%) was purchased from Cambridge Isotope Laboratories. Ultrapure water was filtered by equipment (Millipore, Milli-RO Plus) in the laboratory. All chemicals were used as received without further purification.

Synthesis of Polycrystalline ZnO (p-ZnO) Derived from ZIF-8. ZIF-8 was prepared by microwave-assisted thermal synthesis. Specifically, 9 mmol of zinc acetate dihydrate and 36 mmol of 2-methylimidazole were dissolved in 80 and 100 mL of methanol, respectively, to form solution A and B. Solution A was poured into solution B under vigorous stirring. Subsequently, the resulting mixture was transferred into the microwave chemical reactor (MCR-3) and stirred at 50 °C for 2 h under microwave irradiation. The as-prepared ZIF-8 was collected by centrifugation and washed several times with methanol. After being dried at 60 °C for 12 h, ZIF-8 was transformed to p-ZnO by calcination under air at 450 °C for 3 h with a heating rate of 2 °C·min^{-1}, followed by slow cooling to room temperature.

Synthesis of CuO_X@p-ZnO Derived from Cu-Doped ZIF-8 (Cu-ZIF-8). For the synthesis of Cu-ZIF-8, the identical procedure was employed as described for ZIF-8, except for the introduction of Cu^{2+} to solution A (3 mmol of copper nitrate and 6 mmol of zinc acetate dihydrate in 80 mL of methanol). The collected Cu-ZIF-8 was then transformed into CuO_X@p-ZnO via an identical thermal procedure as for p-ZnO.

Characterization. Transmission electron microscopy (TEM) images, high-resolution transmission electron microscopy (HRTEM) images, and energy dispersive X-ray (EDX) analysis elemental maps were taken on a JEOL-2100F microscope operating at an accelerating voltage of 200 kV. X-ray diffraction (XRD) patterns were obtained on a Bruker D8 Focus X-ray diffractometer with Cu Kα radiation (λ = 1.5405 Å). X-ray photoelectron spectroscopy (XPS) was conducted on a VG ESCALAB MKII X-ray photoelectron spectrometer with a non-monochromatized Al Kα X-ray source ($h\nu$ = 1486.7 eV). X-ray absorption fine structure spectra (XAFS) were obtained at the Beijing Synchrotron Radiation Facility (1W1B). UV−vis absorbance spectra were acquired on a Hitachi U-3900 spectrometer.

Activity Tests of Photocatalytic CO_2 Reduction on p-ZnO and CuO_X@p-ZnO. The photocatalytic CO_2 reduction performance for each sample was evaluated with a 300 W Xe lamp (Perfect Light, Microsolar 300, 320−780 nm, 100 mW·cm^{-2}) as the light source. In a typical activity test, 5 mg of the photocatalyst was dispersed in deionized water and then dripped onto a microfiber paper 3 cm in diameter (Whatman, QMA 1851-047). After naturally drying in the air, the microfiber paper loaded with the photocatalysts was placed in a 100 mL reactor equipped with a quartz window on the top. Prior to irradiation, the photoreactor was subjected to vacuum pumping three times and then refilled by flowing water-vapor-saturated CO_2 gas until

https://dx.doi.org/10.1021/jacs.1c00206
J. Am. Chem. Soc. 2021, 143, 2984−2993

the pressure reached 0.5 MPa. During the reaction, the gas products were analyzed by a gas chromatograph (GC7920-TF2Z) equipped with thermal conductivity and flame ionization detectors, by which H_2, CO, CH_4, C_2H_4, and C_2H_6 are well-resolved. $^{13}CO_2$ isotope labeling experiments were conducted under the same conditions, except though triethylamine (50 vol % in water) as an extra sacrificial agent to enhance the yield of the CO_2 reduction products, and the gas products were quantified by GC−MS (gas chromatography−mass spectrometry, Agilent Technologies 7890A-5957C) with a triple-axis detector.

In Situ FT-IR Measurement. In situ FT-IR spectra were collected on a Bruker Vertex 70 V FT-IR spectrometer equipped with a narrow-band HgCdTe detector and a transmission reaction chamber (Harrick) connected to an evacuation line ($\sim 10^{-7}$ mbar). Five milligrams of the sample powder were pressed into a self-supported pellet (7.0 mm in diameter) and placed in the transmission chamber. In a typical in situ FT-IR measurement, 0.375% CO (diluted by N_2) was first introduced as a probe to identify the states of the surface Cu sites. Then, the transmission chamber was evacuated to remove all of the adsorbed and gaseous CO and subsequently purged with water-vapor-saturated 25% CO_2 ($^{12}CO_2$ or $^{13}CO_2$, diluted by N_2) gas flow. After the equilibrium of CO_2 and water adsorption on the catalyst pellet was reached, the transmission chamber was sealed for the subsequent photocatalytic reactions. A 100 mW continuous diode laser (355 nm) was employed as the light source, and a chopped illumination program with 180 cycles of 20 s illumination and 6 s dark was performed by periodically intercepting the laser beam with a mechanical shutter (Vincent Associates, model Uniblitz). The shutter was controlled by a BNC pulse/delay generator model 565 and synchronized with the data acquisition in an FT-IR spectrometer. The operando IR spectrum with a spectral resolution of 4 cm^{-1} and scanning velocity of 160 Hz was collected in each 6 s dark period of the chopped illumination program. Finally, after the photocatalytic reaction, the chamber was evacuated and then purged with 0.375% CO again to explore the changes in the surface Cu sites.

Calculation Details. The first-principles calculations were carried out with the Vienna ab initio simulation package (VASP).[28−30] The interaction between ions and valence electrons was described by using projector augmented wave (PAW) potentials, and the exchange−correlation between electrons was treated using the generalized gradient approximation (GGA) in the Perdew−Burke−Ernzerhof (PBE) form.[31,32] Moreover, the van der Waals interactions are also taken into account using DFT-D_2 corrections.[33,34] The plane wave cutoff energy was 400 eV and a 2 × 2 × 1 sheet *k*-point mesh was used. The Γ-point was used for gas-phase molecules. Ionic relaxations were carried out under conventional energy (10^{-5} eV) and force (0.03 eV $Å^{-1}$) convergence criteria. Since conventional density functional theory (DFT) functionals are unable to describe the strong correlation effect among the partially filled Cu 3d states in Cu_2O@CuO, the Hubbard parameter, *U*, is introduced for Cu 3d electrons to describe the on-site Coulomb interaction, giving the well-known GGA + *U* method. The values of $U = 7$ eV and $J = 0$ eV were used for the Cu_2O@CuO material and spin-polarized calculations were performed since bulk Cu_2O@CuO has an anti-ferromagnetic ground state.[35] $Cu_2O(111)$ and CuO(111) are the most stable low-index surfaces of the Cu_2O and CuO crystals, which could best represent the surface properties, consistent with previous theoretical results.[20,35] For the original Cu_2O, the $Cu_2O(111)$ model was established with nine atomic layers, including three copper atomic layers and six oxygen atomic layers. Each copper atomic layer was sandwiched by two oxygen atomic layers.[36] For the Cu_2O@CuO model, CuO(111) was first established to be composed of nine atomic layers, including three copper atomic layers and six oxygen atomic layers, and then half of the oxygen atoms on the surface layers of CuO(111) were removed to simulate the feature of the reduced surface Cu^+ upon CuO matrix (Cu_2O@CuO).[37] These models were further expanded by the supercell method into a 2 × 2 cell. A 15 Å vacuum layer was placed above the surface slab to avoid the interference from imaging surface slabs.[38] The adsorption energy (E_{ad}) denotes the interaction between the surface and is defined as $E_{ad} = E_{ads} + E_{sur} - E_{sys}$, where E_{ads} is the energy of the adsorbate before adsorption, E_{sur} is the energy of the surface before adsorption, and E_{sys} is the energy of the system after adsorption. Gibbs free energies for each gaseous and adsorbed species were calculated at 298 K, according to the expression $G_E = E_{DFT} + E_{ZEP} - TS$, where E_{DFT} is the electronic energy calculated with VASP, E_{ZPE} is the zero-point energy, and *TS* is the entropy contribution.[39]

RESULTS

p-ZnO was prepared by the aerobic thermal treatment of pristine ZIF-8, while the hybrid CuO_X@p-ZnO photocatalyst was obtained via the identical pyrolysis procedure but from Cu-doped ZIF-8 (Cu-ZIF-8). For Cu-ZIF-8, some of the Zn^{2+} in ZIF-8 were replaced by Cu^{2+}, as indicated by the overall right shift of the characteristic XRD peaks [Figure S1a, Supporting Information (SI)], while the dodecahedral topography remained the same as that of ZIF-8 (Figure S2, SI). After the aerobic pyrolysis, the XRD patterns of the as-prepared CuO_X@p-ZnO and p-ZnO (Figure S1b, SI) demonstrated the collapse of the topological structure of Cu-ZIF-8 and ZIF-8 and the formation of the metal oxides. All characteristic diffraction peaks of ZnO were observed in both CuO_X@p-ZnO and p-ZnO,[40] and in the former one, in addition to the ZnO peaks, the characteristic peaks at $2\theta = 35.4°$ and 38.7° can be readily assigned to the (002) and (111) planes of CuO, respectively,[41] which indicated that the Cu in CuO_X@p-ZnO mainly existed in the form of CuO. The dominant Cu^{2+} valence state was also revealed by the Cu 2p XPS spectrum in Figure S3a (SI) by the observation of satellite features at 943.0 eV.[42]

On the basis of TEM images in Figures 1a and S4a (SI), after pyrolysis, both CuO_X@p-ZnO and p-ZnO maintained

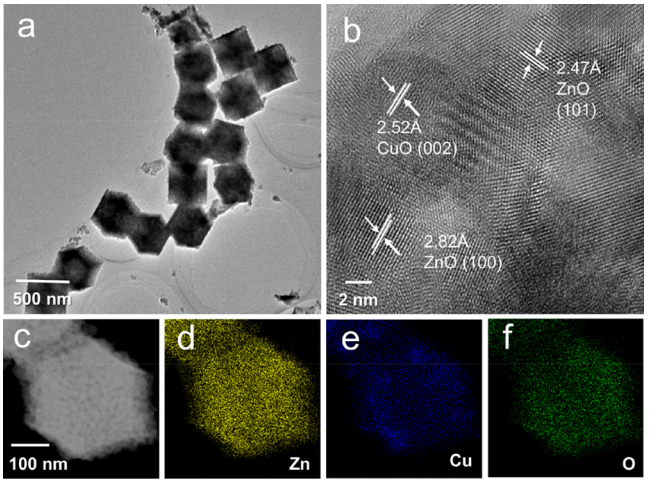

Figure 1. (a) TEM, (b) HRTEM, (c) annular dark-field TEM images, and (d−f) the corresponding elemental mapping images of CuO_X@p-ZnO.

their dodecahedral topography from the Cu-ZIF-8 and ZIF-8 precursors. The HRTEM (Figure S4b, SI) of p-ZnO showed that the dodecahedron was made up of ZnO nanoparticles with different orientations. In the hybrid CuO_X@p-ZnO (Figure 1b), CuO_X nanoparticles were well-dispersed among the ZnO nanoparticles. The EDX elemental mapping (Figure 1c−f) further indicated such uniform distribution of Cu and Zn in the hybrid catalyst, and the atomic concentrations of Cu and Zn in the near-surface region were calculated to be 7.32 and 42.24 atom %, respectively, with a Cu/Zn atomic ratio of

https://dx.doi.org/10.1021/jacs.1c00206
J. Am. Chem. Soc. 2021, 143, 2984−2993

nearly 1:6 (Figure S5, SI). Since the feeding Cu/Zn ratio in the reactants was 1:1, this would suggest that the current incorporation of Cu in the CuO_X@p-ZnO hybrid catalyst had reached the maximum. The C elemental mapping (Figures S4e and S6, SI) showed that only trace amounts of C remained after the aerobic calcination, while N, another element from the organic framework of the ZIF precursor, was not detected, since no notable N 1s peak was observed in the XPS spectra (Figure S7, SI), demonstrating that the vast majority of the organic frameworks was transformed to gaseous products and was removed from the photocatalyst during the aerobic pyrolysis. On the basis of all these characterizations, it can be determined that through the aerobic thermal treatment of the Cu-ZIF-8 precursor, a hybrid catalyst with uniformly dispersed Cu in the ZnO matrix was obtained.

Then the photocatalytic CO_2 reduction performance on p-ZnO and CuO_X@p-ZnO was also tested. As shown in Figure 2a, in the presence of water vapor, the only CO_2 reduction

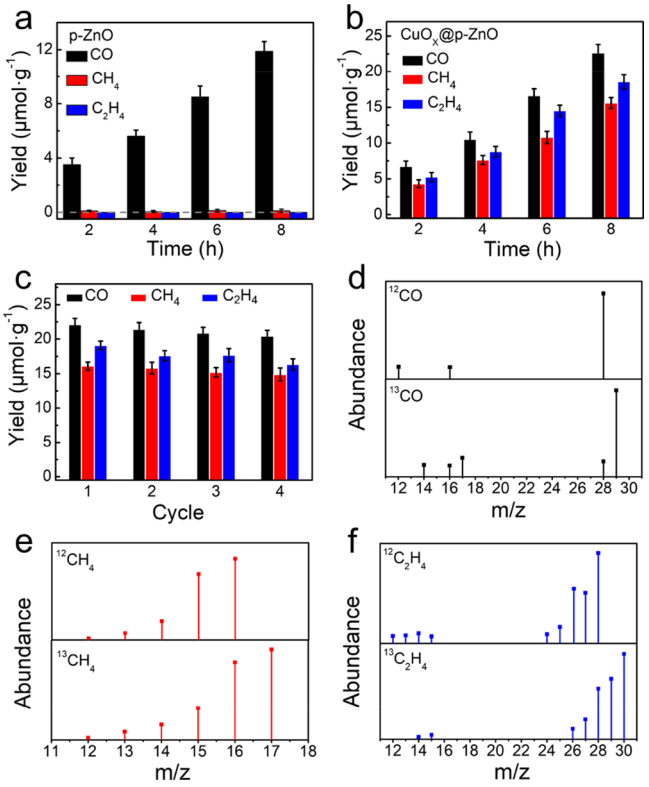

Figure 2. Products of photocatalytic CO_2 reduction for (a) CuO_X@p-ZnO and (b) p-ZnO; error bars represent the SD of three independent measurements using 5 mg of fresh sample for each measurement. (c) Cycling measurements for CO_2 photoreduction of CuO_X@p-ZnO (using a 5 mg sample for this measurement; when a new catalytic cycle begins, the reactor is pumped and refilled with pure CO_2 and H_2O). GC−MS spectra of (d) CO, (e) CH_4, and (f) C_2H_4 from the photocatalytic reduction of $^{12}CO_2$ or $^{13}CO_2$ on CuO_X@p-ZnO.

product on p-ZnO upon illumination was CO, which accumulated linearly with the reaction time at a rate of 1.8 $\mu mol \cdot g^{-1} \cdot h^{-1}$, and no CH_4 or C_2H_4 was detected during the 8 h illumination period. On CuO_X@p-ZnO (Figure 2b), under identical conditions, the rate of generation of CO was almost doubled, with an average generation rate of 3.3 $\mu mol \cdot g^{-1} \cdot h^{-1}$. More intriguingly, multielectron-reduced hydrocarbons of CH_4 and C_2H_4 were also detected; the evolution of the latter has rarely been reported in photocatalytic systems. The generation rates of CH_4 and C_2H_4 were of the same magnitude as that of CO at rates of 2.2 and 2.7 $\mu mol \cdot g^{-1} \cdot h^{-1}$, respectively. The selectivity of hydrocarbon production reached 59.8%, and the C_2H_4 production selectivity was 32.9%. H_2 was not detected in our gas−solid reaction system, which could originate from the advantages in the reagent concentration of gaseous CO_2 compared to water vapor in the gas−solid reaction that remarkably pressed the H_2 production.[4] On both p-ZnO and CuO_x@p-ZnO, the generation of O_2 was detected (Figure S9, SI), consolidating the role of water vapor as hole scavenger during the photocatalytic reactions. The hybrid catalyst exhibited excellent stability over reaction time; the cycling experiment demonstrated that even in the fourth cycle of photoreactions (Figure 2c), the yield of each CO_2 reduction product remained >90% of that in the first cycle, and the overall selectivity of hydrocarbons also remained constant.

The activity test was also performed in the presence of triethylamine (TEA) as a sacrificial agent (Figure S10, SI). Since TEA is a better hole scavenger than water, it should facilitate the separation of the photogenerated carriers and then enhance the density of the photogenerated electrons. In the presence of TEA, the photocatalytic CO_2 reduction significantly accelerated on both p-ZnO and CuO_X@p-ZnO. On p-ZnO, the generation rate of CO increased to 9.3 $\mu mol \cdot g^{-1} \cdot h^{-1}$. It is worth noting that with the enhanced electron density, multielectron-reduced CH_4 (2.1 $\mu mol \cdot g^{-1} \cdot h^{-1}$) was formed, suggesting again that the electron density is the bottleneck for the photocatalytic CO_2 reduction to hydrocarbon. In sharp contrast, despite the enhanced electron densities in the presence of TEA, C_2H_4 with more sluggish generation kinetics was still absent on p-ZnO, stressing the irreplaceable role of the CuO_X moiety in the formation of C_2H_4. On CuO_X@p-ZnO, regardless of the remarkably enhanced yield for each CO_2 reduction product (CO, 27.3 $\mu mol \cdot g^{-1} \cdot h^{-1}$; CH_4, 17.9 $\mu mol \cdot g^{-1} \cdot h^{-1}$; and C_2H_4, 22.3 $\mu mol \cdot g^{-1} \cdot h^{-1}$), the product distribution was still the same as that in the absence of TEA, which suggested that the addition of TEA enhanced only the reaction rate but did not changed the reaction pathway.

A series of control experiments were perfomed to determine the origin of the CO_2 reduction products on CuO_X@p-ZnO. As shown in Figure S11 (SI), after a 12 h reaction, no CO or hydrocarbon products were detected when the reaction system was in absence of illumination, catalyst, or CO_2, separately. Trace products (<0.02 $\mu mol \cdot g^{-1} \cdot h^{-1}$) were detected when replacing the water-saturated CO_2 atmosphere with dry CO_2, since the limited amounts of the adsorbed water on the catalyst may act as hole scavengers. The experiment using isotope-labeled $^{13}CO_2$ was also conducted with TEA as a hole scavenger, and the products were measured by GC−MS. The GC−MS peak sequences of CO, CH_4, CO_2, and C_2H_4 are shown in Figure S12 (SI), and the ion fragment analysis results of each peak are displayed in Figure 2d−f. The ion fragment peaks for CO, CH_4, or C_2H_4 under $^{13}CO_2$ were clearly shifted compared with those under $^{12}CO_2$, demonstrating that the generated CO and hydrocarbons on CuO_X@p-ZnO were definitely derived from the reduction of CO_2 rather than other sources.

Regardless of the identity of the hole scavenger in the system, the comparison of the performance of CuO_X@p-ZnO and p-ZnO in photocatalytic CO_2 reduction clearly demon-

https://dx.doi.org/10.1021/jacs.1c00206
J. Am. Chem. Soc. 2021, 143, 2984−2993

strates the key role of the CuO_X moiety in the formation of hydrocarbons, especially the C−C coupling products of C_2H_4. Therefore, further mechanistic exploration was conducted to understand the origin of the extraordinary activities of C_2H_4 generation on our CuO_X@p-ZnO photocatalyst.

Since the catalytic behaviors of CO_2 reduction on Cu could be significantly affected by the oxidation states of Cu, the stabilized valence state of Cu during photocatalytic CO_2 reduction on CuO_X@p-ZnO was first determined. XPS and XAFS characterizations were employed to identify the valence state of Cu in the hybrid photocatalyst that occurred during different reaction times. According to Cu 2p XPS data (Figure S13, SI), as the reaction progressed, the characteristic peak of Cu^{2+} at 933.5 eV slightly shifted to a lower binding energy, which would indicate the partial reduction of Cu^{2+} to Cu^+.[43] The shift was more prominent within the first 4 h, while no further alternations in the shape of the ∼933.5 eV peak occurred when the illumination prolonged, suggesting that no more transformation from Cu^{2+} to Cu^+ transpired when the illumination time exceeded 4 h. On the other hand, the retained collection satellite features at 943.0 eV characteristic for CuO after 10 h reactions would suggest that the majority of Cu^{2+} was unchanged during the illumination and only a small fraction was reduced to Cu^+.

The more definitive evidence for this judgment was from semi-in-situ XAFS characterization. Cu K-edge X-ray absorption near-edge structure (XANES) spectra for the hybrid CuO_X@p-ZnO collected after different reaction times are shown in Figure 3a, and as a comparison, the reference spectra

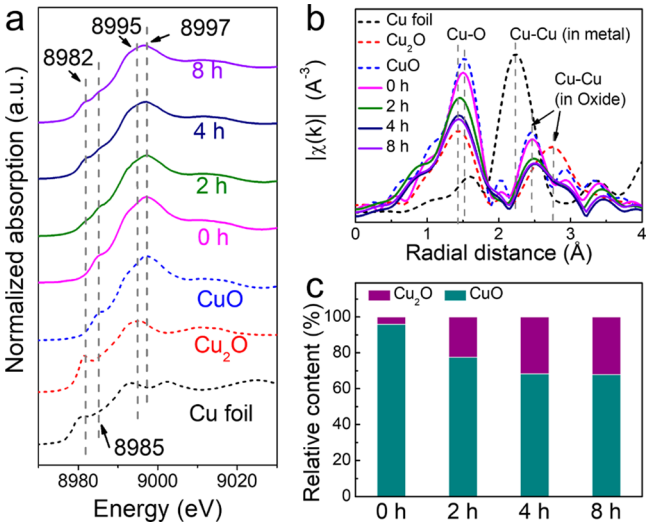

Figure 3. (a) Copper K-edge X-ray absorption near-edge structure (XANES) spectra on pristine Cu^0 foil, Cu_2O, CuO, and CuO_X@p-ZnO collected after 0, 2, 4, and 8 h photoreactions. (b) Fourier-transformed K^2-weighted $\chi(k)$ function of EXAFS and (c) relative content of CuO and Cu_2O on CuO_X@p-ZnO after 0, 2, 4, and 8 h photoreactions.

collected on standard CuO, Cu_2O, and Cu foil are also exhibited. The original catalyst (0 h) mainly showed the characteristic peaks of CuO at 8985 and 8997 eV, assigned to 1s → $4p_z$ and 1s → $4p_{x,y}$ of Cu^{2+}, respectively.[44,45] As the reaction time increased (2 and 4 h), the characteristic shoulder peak of Cu_2O at 8982 eV, assigned to 1s → $4p_z$ of Cu^+, became prominent; meanwhile, the characteristic peak of CuO at 8997 eV slightly shifted to 8995 eV, ascribed to 1s → $4p_{x,y}$ of Cu^+.[44,46] Similar to the XPS results, the variations between the 8 and 4 h XANES spectra were unnoticeable, and when comparing between the 8 and 0 h spectra, the main characteristic CuO features were retained. The result was further verified by the Fourier-transformed K^2-weighted $\chi(k)$ function of EXAFS. As exhibited in Figure 3b, before photoreaction, the main backscattering peak of CuO_X@p-ZnO around 1.5 Å corresponded to the Cu−O shell in CuO, and as the reaction progressed, the peak gradually shifted to smaller radial distance, indicating the partial reduction of Cu^{2+}, since Cu_2O has the main Cu−O peak at 1.4 Å. It should be noted that, after 4 h photoreactions, the average Cu−O distance in CuO_X@p-ZnO was very close to that in pristine Cu_2O, whereas the shift in the average distance of the Cu−Cu shell was quite limited and still closer to that in pristine CuO. Such a discrepancy would suggest that the structure of the in situ formed surface Cu_2O layers is distinctive from the pure lattice of Cu_2O: the reduction of the original CuO surface layer leads to the removal the surface O atom, resulting in the variation in the average distance of the Cu−O shell, but the Cu^{2+} reduction should be limited to the surface layer; therefore, the surface Cu atoms can be still anchored to the bulk CuO matrix with subsurface O atoms, and then the change in the distance of the Cu−Cu shell should not be remarkable.[43,45]

On the basis of the fitting of data in Figure 3a (Figures S14−17, SI), Figure 3c revealed the time-dependent variations of the relative contents of CuO and Cu_2O in the near-surface region of the samples: the relative content of Cu_2O increased from the original 4.1% to 22.5% after 2 h and 31.8% after 4 h, but the difference between the content at 4 and 8 h (32.1%) was quite small.

According to the XPS and XAFS data, it can be clearly concluded that, as the reaction progressed, the surface Cu^{2+} in CuO_X@p-ZnO was reduced to Cu^+, and the Cu^{2+} reduction was more significant in the first 2 h and came to an end after 4 h. Then, the most possible structure of the CuO_X moiety after stabilization would be the reduced surface Cu^+ layer on the CuO matrix. Despite the conduction band level of ZnO being sufficiently high to fully reduce Cu^{2+} to Cu^+ and even Cu^0,[47] the majority of Cu in the hybrid catalyst still exists in the form of CuO, and the most likely explanation is the competition between Cu^{2+} reduction and CO_2 reduction on the catalyst surface that impeded further reduction of the Cu^{2+} in the subsurface layer and bulk. The detailed reaction mechanism will be subsequently explored by in situ FT-IR spectra.

Time-dependent in situ FT-IR spectra collected during photocatalytic reactions are employed not only to identify the reaction intermediate from the IR absorption features but also to trace the generation kinetics of both intermediates and products, which provides additional information to uncover the detailed reaction mechanism.[48−51] Before and after the in situ photocatalytic reactions, external CO molecules were introduced as probes. CO probes are frequently combined with infrared spectra to identify the states of the surface sites, as the IR vibration frequency of bound CO is very sensitive to the valence state and coordination environment of the surface metal atoms.[23,52,53] As shown in Figure 4a, when CO probes were introduced before the photocatalytic reaction, only one band from the adsorbed CO was observed on CuO_X@p-ZnO at 2085 cm^{-1}. Since no CO band was obtained on ZnO, this band should be assigned to the CO adsorbed on the CuO_X moiety.[58] The frequency of CO coordinated to Cu^{2+} was

https://dx.doi.org/10.1021/jacs.1c00206
J. Am. Chem. Soc. 2021, 143, 2984−2993

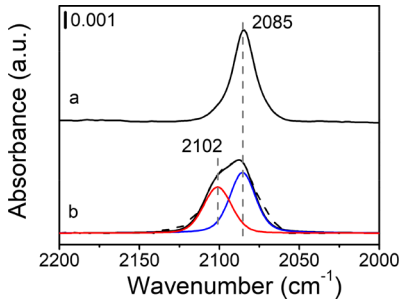

Figure 4. Identification of surface Cu sites on CuO_X@p-ZnO with CO as a molecular probe: adsorption of CO before (a) and after (b) 1 h of chopped illumination (the black dashed line is the original absorption peak, and the other lines are the fitted peaks). The background for both spectra was the one collected on CuO_X@p-ZnO under vacuum before the photocatalytic reaction. For clarification, the P and R branches at 2173 and 2120 cm^{-1} for gaseous CO were subtracted using the standard spectra collected from the sample-free chamber containing an identical concentration of gaseous CO.

reported to be in the region of 2200−2190 cm^{-1}; however, due to the weak interaction with Cu^{2+}, such a band was not observed here.[54,55] The 2085 cm^{-1} band can be attributed to CO adsorption on the minor Cu^+ sites (Cu^+_{2085}) that originally existed in the CuO_X@p-ZnO catalyst.[56] When the in situ photocatalytic reactions were ended, the reaction chamber was evacuated and filled with external CO probe again to identify the changes on the surface sites after reactions. As shown in Figure 4b, besides the 2085 cm^{-1} band, another band at 2102 cm^{-1} was observed, which can be assigned to adsorbed CO on newly formed Cu^+ that is under different coordination circumstance with regard to Cu^+_{2085}. Corresponding to the XAFS and XPS results, this in situ formed $Cu_{2102}{}^+$ should be originating from the photocatalytic reduction of the surface layer Cu^{2+} in CuO_X@p-ZnO.

The CO probe experiment displays accordant results with XAFS and XPS for the in situ generation of surface Cu^+ sites in CuO_X@p-ZnO, and then the detailed reaction procedure was uncovered by analyzing the in situ IR spectra collected during the chopped illuminations. A chopped illumination program synchronized with in situ FT-IR measurements was employed, as shown in Figure 5A. In each illumination−measurement cycle, one IR spectrum was collected after 20 s of illumination.

As a control, photocatalytic CO_2 reduction on p-ZnO was first explored. As shown in Figure 5B-a, illumination by a 355 nm laser induced an IR featureless background absorbance that monotonically increased from 4000 to 1250 cm^{-1}, which was intensified with prolonged illumination. A similar background shift has been reported on TiO_2 and was assigned to the accumulation of photogenerated electrons in the conduction band.[57] Simultaneously, with the increase in the background absorbance, depletions at 1416, 1518, and ∼3190 cm^{-1} are observed. There should be another diminished band at approximately 1643 cm^{-1} that is blurred by the dramatically increasing background absorbance (which was more prominent on CuO_X@p-ZnO in Figures 5B-b and 6). These depletion bands can be all assigned to the adsorbed water molecules on p-ZnO: the broad band centered at 3190 cm^{-1} for the O−H stretching vibration (ν_{OH}), the 1643 cm^{-1} band for the bending vibration of the molecular adsorbed water (δ_{H2O}), and the 1518 and 1416 cm^{-1} bands for the bending vibration of the dissociated adsorbed water (δ_{Zn-OH}).[58,59] Additionally, considering the relatively low CO_2 reduction rate

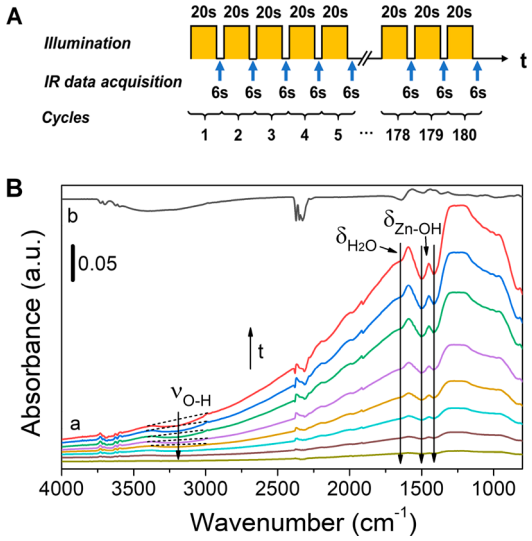

Figure 5. (A) The chopped illumination program synchronized with the in situ FT-IR measurement for both ZnO and CuO_X@ZnO. (B) (a) In-situ FT-IR spectra of the photocatalytic CO_2 reduction on ZnO recorded during illumination cycles of 1, 4, 10, 20, 40, 80, 120, and 180 (bottom to top); (b) the FT-IR spectrum collected on CuO@ZnO in the 180th illumination cycle exhibited for the convenience of comparison. The background was collected immediately right before illumination for each sample.

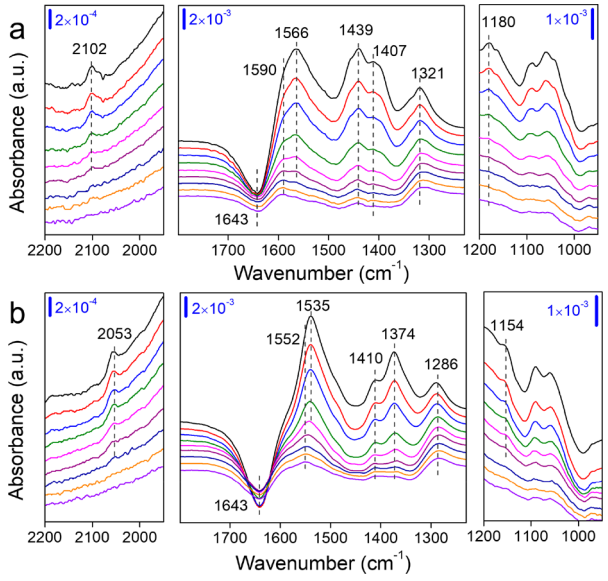

Figure 6. In situ FT-IR spectra of the photocatalytic (a) $^{12}CO_2$ or (b) $^{13}CO_2$ reduction on CuO_X@p-ZnO recorded in the illumination cycle of 1, 2, 4, 10, 20, 40, 80, 120, and 180 (bottom to up).

on p-ZnO in the activity test, it is suggested that on p-ZnO, water oxidation was much faster than the CO_2 reduction half of the reaction; therefore, since the holes and electrons were generated stoichiometrically, the dramatic consumption of holes by water oxidation leaves the residual electrons accumulated in the conduction band, observed as the background shift in the infrared spectra.

However, such an increase in the IR background absorbance disappeared when applying the identical illumination program on CuO_X@p-ZnO, as indicated by the sharp contrast between Figure 5B-b and the top curve in Figure 5B-a, which are the

https://dx.doi.org/10.1021/jacs.1c00206
J. Am. Chem. Soc. 2021, 143, 2984−2993

infrared spectra collected in the 180th illumination cycle on CuO_X@p-ZnO and p-ZnO, respectively. The lack of accumulated electrons indicated the efficient electron transfer from the p-ZnO to the CuO_X moiety, and the latter part acted as the reduction reaction center to rapidly consume the electrons for either the reduction of the adsorbed CO_2 or the self-reduction to Cu^+.[57] On the basis of this consideration, on CuO_X@p-ZnO, all of the observed CO_2-reduction-related IR bands should be attributed to the intermediates or products on the CuO_X moiety rather than the p-ZnO moiety.

The variations in the infrared spectra with the illumination time on CuO_X@p-ZnO are shown in Figure 6a, while in Figure 6b, $^{13}CO_2$ was used instead of $^{12}CO_2$. It can be observed that, during illumination, the depletion of the molecular adsorbed water at 1643 cm^{-1} was greater than that on p-ZnO and was intensified with prolonged illumination, confirming the consumption of water molecules as hole scavengers. On the other hand, in Figure 6a, the growth of the IR bands at 1590, 1439, and 1321 cm^{-1} was prominent even from the first cycle of illumination, and all of the three bands had their ^{13}C-counterparts at 1552, 1410, and 1286 cm^{-1}, respectively (Figure 6b). According to the literature reports, we would assign the 1552 and 1286 cm^{-1} bands to the asymmetric and symmetric vibration of surface-adsorbed carbonate, while the 1439 cm^{-1} band could be attributed to the one-electron-reduced *COOH.[22,23,60]

In the initial stage of the photocatalytic reactions, no CO band was observed in the region of 2200−2000 cm^{-1}; after only an induction period of 10 cycles of illumination, the IR band of Cu^+−CO at 2102 cm^{-1} with its ^{13}C-counterpart at 2053 cm^{-1} became notable and grew sharply under the subsequent illuminations. The appearance of 2102 cm^{-1} bands gave two indications: first, the Cu_{2102}^+ was generated; second, it thereafter acted as the reaction center to reduce CO_2 to CO, and then the generated CO was subsequently in situ trapped. Intriguingly, no CO band at 2085 cm^{-1} was detected during the whole photocatalytic reaction processes, suggesting that the in situ generated Cu_{2102}^+ was a more reactive surface site for CO_2 reduction than the originally existing Cu_{2085}^+.

Almost simultaneously with the appearance of Cu^+−CO at 2102 cm^{-1} was the change in the IR features in the region of 1600−1550 cm^{-1} (Figure 6a): a new peak at 1566 cm^{-1} started to grow and the absorption maximum in this region gradually shifted from the carbonate band of 1590 cm^{-1} to this new band with prolonged illumination. The IR bands at 1180 and 1407 cm^{-1} exhibited growth kinetics identical to those of the 1566 cm^{-1} band: an induction period in the first 10 cycles of illumination was also observed. In the $^{13}CO_2$ isotope experiment (Figure 6b), these three bands shifted to 1535, 1374, and 1154 cm^{-1}, respectively, with similar spectral kinetics.

Distinctive with the carbonate or *COOH bands growing without an induction period, the evolution of the CO_2-related bands of 1566, 1407, and 1180 cm^{-1} exhibited growth kinetics similar to that of the Cu_{2102}^+−CO band, suggesting that the formation of these bands needs the generation of Cu_{2102}^+−CO as a premise. Since, in the activity tests under similar reaction conditions, the generation of C_2H_4 and CH_4 was confirmed, both of which were proposed to be further reduced from *CO (Scheme 1), the 1566, 1407, and 1180 cm^{-1} bands could be assigned to the intermediate between *CO and hydrocarbon C_2H_4 or CH_4. The only spectroscopic identification of *OC−COH, one of the C−C coupling intermediates, was by Koper and co-workers, who reported the IR wavenumbers of 1584 cm^{-1} for C═O stretching and 1191 cm^{-1} for C−OH stretching during electrochemical IR measurements on a copper electrode.[52,60] The band positions were very close to their theoretical calculation results of 1576 and 1235 cm^{-1}. The v-QM theoretical calculation of Cu(001) from Goddard and co-workers also predicted similar wavenumbers at 1548 and 1189 cm^{-1},[22] respectively. On the basis of these literature reports and the spectral kinetics observed here, we assigned our 1566 and 1180 cm^{-1} bands with identical growth kinetics to *OC−COH intermediates adsorbed on Cu_{2102}^+, which provides the first experimental identification of a C−C coupling intermediate during the photocatalytic CO_2 reduction. On the other hand, the band at 1407 cm^{-1} has been reported as the IR frequency of *CHO, the most reported intermediate for CH_4, on a copper electrode.[60] It is also correlated to our observed spectral kinetics to assign 1407 cm^{-1} to that active intermediate for CH_4.

DISCUSSION

According to the in situ FT-IR studies, a detailed reaction process on CuO_X@p-ZnO can be proposed. In the initial stage, the surface Cu^{2+} sites on the hybrid catalyst are first reduced to Cu_{2102}^+ by electron transfer from excited p-ZnO. After the surface Cu^{2+} is reduced to Cu^+, which is more active for CO_2 reduction than Cu^{2+}, surface CO_2 reduction on Cu^+ dominates and primarily consumes the electrons transferred from p-ZnO and thus prevents the reduction of Cu^{2+} in the subsurface layer and bulk; therefore, a specific structure of a Cu^+ surface layer upon the CuO matrix is formed, as proven by the XAFS and CO probing experiments. For the CO_2 reduction conducted on Cu_{2102}^+, after the two-electron reduction to CO, some part of the generated *CO desorbed to form gaseous CO, and other *CO species were trapped on Cu_{2102}^+, leading to subsequent electron transfer to further reduce the surface-bound *CO into CH_4 and C_2H_4 via the intermediates *CHO and *OC−COH, respectively.

On the basis of this proposition, theoretical calculations were conducted to determine whether such a specific structure of surface Cu^+ sites favored the formation of C_2H_4. To simulate the C−C coupling step on the CuO_X catalyst with mixed Cu(I)/Cu(II) valence states, half of the O atoms were removed from the surface slab of CuO(111) to form the surface layers of Cu^+(Cu_2O@CuO), which is consistent with the EXAFS results, while the ordinary Cu_2O(111) structure was employed as a comparison (Figure S18, SI). As shown in Figure 7, the adsorption energy of *CO on Cu_2O@CuO (3.29

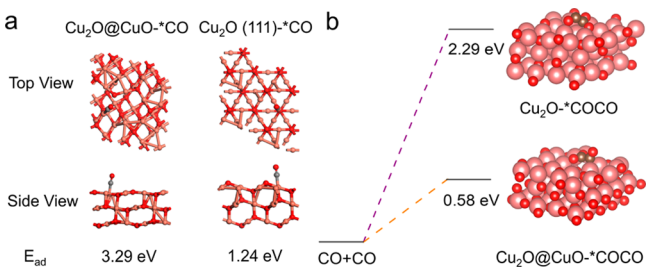

Figure 7. (a) The initial ball-and-stick structural models of the theoretical calculations of the adsorption energy of *CO on pristine Cu_2O and Cu_2O@CuO. (b) First-principles calculations of the C−C coupling step for Cu_2O and Cu_2O@CuO. Color code: Cu, pink; O, red; C, gray.

https://dx.doi.org/10.1021/jacs.1c00206
J. Am. Chem. Soc. 2021, 143, 2984−2993

eV) is significantly higher than that on ordinary Cu_2O (1.24 eV) (Figure 7a), and the change in the Gibbs free energy (ΔG) for the formation of the *OC−CO intermediate on Cu_2O@CuO (0.58 eV) is far smaller than the ΔG of 2.29 eV on pristine $Cu_2O(111)$ (Figure 7b). Therefore, it verifies that compared with Cu^+ in the pure Cu_2O lattice, the in situ generated surface Cu^+ upon the CuO matrix in CuO_X@p-ZnO should be more conducive to both the trapping of CO and the subsequent formation of key intermediates in the C−C coupling. The strengthened binding of *CO and the remarkable reduced formation energy of the C−C coupling intermediate during the CO_2 reduction are both critical to achieve the formation of C_2H_4 in the photocatalytic system: the former prolongs the residence time of *CO on the catalytic center, and the latter suggests the acceleration in the critical but sluggish step of C−C coupling, both of which guarantee the completion of the multielectron reduction of *CO before it releases from the catalytic sites, especially when considering the relatively slower electron transfer rate in the photocatalytic system. Thus, the theoretical calculations further confirmed that the structure of in situ generated Cu^+ in CuO_X@p-ZnO played a vital role in the photocatalytic CO_2 reduction to C_2H_4.

CONCLUSION

With Cu-doped ZIF-8 as a precursor, a photocatalyst with uniformly dispersed copper oxide among polycrystalline ZnO is synthesized, and upon illumination, this catalyst exhibits the capability to reduce CO_2 to the hydrocarbons CH_4 and C_2H_4. This ability has rarely been achieved in photocatalytic systems. The self-preactivation in the initial stage of photocatalysis builds up the unique surface reaction sites: the surface Cu^{2+} is reduced to a Cu^+ surface layer upon the CuO matrix, and such a structure has been demonstrated to be critical for trapping the in situ generated CO and the subsequent catalytic C−C coupling for C_2H_4 production. Further improvement in the efficiency of CO_2 reduction to C_2H_4 can be expected by optimizing the assembling of the semiconductor sensitizer and CuO_X cocatalyst. Our study sheds light on the roles of the valence state of Cu in tuning the reaction pathway of CO_2 reduction and opens up a new paradigm to achieve the reduction of CO_2 to C_{2+} hydrocarbons in a photocatalytic system.

ASSOCIATED CONTENT

Supporting Information

The Supporting Information is available free of charge at https://pubs.acs.org/doi/10.1021/jacs.1c00206.

XRD patterns; TEM images; XPS spectra; EDX; element distribution of C; VB-XPS spectra; O_2 evolution during the photocatalytic CO_2 reduction; yield of each CO_2 reduction; reaction behaviors in the CuOX@p-ZnO system; GC−MS spectra peak sequence of CO, CH_4, CO_2, and C_2H_4 during the photocatalytic CO_2 reduction; fitting of relative content of CuO and Cu_2O to XANES spectra; and the initial structural models of Cu_2O, Cu_2O−CuO, Cu_2O−*OCCO, and Cu_2O@CuO−*OCCO (Figures S1−S19 and Table S1) (PDF)

AUTHOR INFORMATION

Corresponding Author

Hua Sheng − *Key Laboratory of Photochemistry, Institute of Chemistry, Chinese Academy of Sciences, Beijing 100190, PR China; University of Chinese Academy of Sciences, Beijing 100190, PR China;* orcid.org/0000-0002-5605-2630; Email: hsheng@iccas.ac.cn

Authors

Wei Wang − *Key Laboratory of Photochemistry, Institute of Chemistry, Chinese Academy of Sciences, Beijing 100190, PR China; University of Chinese Academy of Sciences, Beijing 100190, PR China*

Chaoyuan Deng − *Key Laboratory of Photochemistry, Institute of Chemistry, Chinese Academy of Sciences, Beijing 100190, PR China; University of Chinese Academy of Sciences, Beijing 100190, PR China*

Shijie Xie − *Key Laboratory of Photochemistry, Institute of Chemistry, Chinese Academy of Sciences, Beijing 100190, PR China; University of Chinese Academy of Sciences, Beijing 100190, PR China*

Yangfan Li − *Key Laboratory of Photochemistry, Institute of Chemistry, Chinese Academy of Sciences, Beijing 100190, PR China; University of Chinese Academy of Sciences, Beijing 100190, PR China*

Wanyi Zhang − *Key Laboratory of Photochemistry, Institute of Chemistry, Chinese Academy of Sciences, Beijing 100190, PR China; University of Chinese Academy of Sciences, Beijing 100190, PR China*

Chuncheng Chen − *Key Laboratory of Photochemistry, Institute of Chemistry, Chinese Academy of Sciences, Beijing 100190, PR China; University of Chinese Academy of Sciences, Beijing 100190, PR China;* orcid.org/0000-0003-4034-8063

Jincai Zhao − *Key Laboratory of Photochemistry, Institute of Chemistry, Chinese Academy of Sciences, Beijing 100190, PR China; University of Chinese Academy of Sciences, Beijing 100190, PR China;* orcid.org/0000-0003-1449-4235

Complete contact information is available at: https://pubs.acs.org/10.1021/jacs.1c00206

Notes

The authors declare no competing financial interest.

ACKNOWLEDGMENTS

This work was supported by the National Key Research and Development Program of China (No. 2020YFA0710303), the National Natural Science Foundation of China (Nos. 22076193 and 21827809), and the "Strategic Priority Research Program B" of the Chinese Academy of Sciences (Grant No. XDB36000000). The authors thank the photoemission beamline 1W1B station of the Beijing Synchrotron Radiation Facility (BSRF) for XAFS measurements.

REFERENCES

(1) Hepburn, C.; Adlen, E.; Beddington, J.; Carter, E. A.; Fuss, S.; Mac Dowell, N.; Minx, J. C.; Smith, P.; Williams, C. K. The Technological and Economic Prospects for CO_2 Utilization and Removal. *Nature* **2019**, *575*, 87−97.

(2) Jiang, Z.; Xu, X.; Ma, Y.; Cho, H. S.; Ding, D.; Wang, C.; Wu, J.; Oleynikov, P.; Jia, M.; Cheng, J.; Zhou, Y.; Terasaki, O.; Peng, T.; Zan, L.; Deng, H. Filling Metal−Organic Framework Mesopores with TiO_2 for CO_2 Photoreduction. *Nature* **2020**, *586*, 549−554.

(3) Xiong, X.; Mao, C.; Yang, Z.; Zhang, Q.; Waterhouse, G. I. N.; Gu, L.; Zhang, T. Photocatalytic CO_2 Reduction to CO over Ni Single Atoms Supported on Defect-Rich Zirconia. *Adv. Energy Mater.* **2020**, *10*, 2002928.
(4) Li, X.; Sun, Y.; Xu, J.; Shao, Y.; Wu, J.; Xu, X.; Pan, Y.; Ju, H.; Zhu, J.; Xie, Y. Selective Visible-Light-Driven Photocatalytic CO_2 Reduction to CH_4 Mediated by Atomically Thin CuIn5S8 Layers. *Nat. Energy* **2019**, *4*, 690−699.
(5) Rao, H.; Schmidt, L. C.; Bonin, J.; Robert, M. Visible-Light-Driven Methane Formation from CO_2 with a Molecular Iron Catalyst. *Nature* **2017**, *548*, 74−77.
(6) Wu, Y. A.; McNulty, I.; Liu, C.; Lau, K. C.; Liu, Q.; Paulikas, A. P.; Sun, C. J.; Cai, Z.; Guest, J. R.; Ren, Y.; Stamenkovic, V.; Curtiss, L. A.; Liu, Y.; Rajh, T. Facet-Dependent Active Sites of a Single Cu_2O Particle Photocatalyst for CO_2 Reduction to Methanol. *Nat. Energy* **2019**, *4*, 957−968.
(7) Nitopi, S.; Bertheussen, E.; Scott, S. B.; Liu, X.; Engstfeld, A. K.; Horch, S.; Seger, B.; Stephens, I. E. L.; Chan, K.; Hahn, C.; Nørskov, J. K.; Jaramillo, T. F.; Chorkendorff, I. Progress and Perspectives of Electrochemical CO_2 Reduction on Copper in Aqueous Electrolyte. *Chem. Rev.* **2019**, *119*, 7610−7672.
(8) Chen, C.; Khosrowabadi Kotyk, J. F.; Sheehan, S. W. Progress toward Commercial Application of Electrochemical Carbon Dioxide Reduction. *Chem* **2018**, *4*, 2571.
(9) Ran, J.; Jaroniec, M.; Qiao, S. Z. Cocatalysts in Semiconductor-Based Photocatalytic CO_2 Reduction: Achievements, Challenges, and Opportunities. *Adv. Mater.* **2018**, *30*, 1704649.
(10) Albero, J.; Peng, Y.; García, H. Photocatalytic CO_2 Reduction to C_{2+} Products. *ACS Catal.* **2020**, *10*, 5734−5749.
(11) Jiang, K.; Sandberg, R. B.; Akey, A. J.; Liu, X.; Bell, D. C.; Nørskov, J. K.; Chan, K.; Wang, H. Metal Ion Cycling of Cu Foil for Selective C−C Coupling in Electrochemical CO_2 Reduction. *Nat. Catal.* **2018**, *1*, 111−119.
(12) Zhou, Y.; Che, F.; Liu, M.; Zou, C.; Liang, Z.; De Luna, P.; Yuan, H.; Li, J.; Wang, Z.; Xie, H.; Li, H.; Chen, P.; Bladt, E.; Quintero-Bermudez, R.; Sham, T. K.; Bals, S.; Hofkens, J.; Sinton, D.; Chen, G.; Sargent, E. H. Dopant-Induced Electron Localization Drives CO_2 Reduction to C_2 Hydrocarbons. *Nat. Chem.* **2018**, *10*, 974−980.
(13) Dinh, C.; Burdyny, T.; Kibria, G.; Seifitokaldani, A.; Gabardo, C. M.; García de Arquer, F. P.; Kiani, A.; Edwards, J. P.; De Luna, P.; Bushuyev, O. S.; Zou, C.; Quintero-Bermudez, R.; Pang, Y.; Sinton, D.; Sargent, E. H. CO_2 Electroreduction to Ethylene via Hydroxide-Mediated Copper Catalysis at an Abrupt Interface. *Science* **2018**, *360*, 783−787.
(14) Wang, G.; He, C. T.; Huang, R.; Mao, J.; Wang, D.; Li, Y. Photoinduction of Cu Single Atoms Decorated on UiO-66-NH_2 for Enhanced Photocatalytic Reduction of CO_2 to Liquid Fuels. *J. Am. Chem. Soc.* **2020**, *142*, 19339−19345.
(15) Wang, Y.; Chen, Z.; Han, P.; Du, Y.; Gu, Z.; Xu, X.; Zheng, G. Single-Atomic Cu with Multiple Oxygen Vacancies on Ceria for Electrocatalytic CO_2 Reduction to CH_4. *ACS Catal.* **2018**, *8*, 7113−7119.
(16) Yuan, L.; Hung, S. F.; Tang, Z. R.; Chen, H. M.; Xiong, Y.; Xu, Y. J. Dynamic Evolution of Atomically Dispersed Cu Species for CO_2 Photoreduction to Solar Fuels. *ACS Catal.* **2019**, *9*, 4824−4833.
(17) Xu, S.; Carter, E. A. Theoretical Insights into Heterogeneous (Photo)Electrochemical CO_2 Reduction. *Chem. Rev.* **2019**, *119*, 6631−6669.
(18) Ozin, G. A. Throwing New Light on the Reduction of CO_2. *Adv. Mater.* **2015**, *27*, 1957−1963.
(19) Wu, J.; Huang, Y.; Ye, W.; Li, Y. CO_2 Reduction: From the Electrochemical to Photochemical Approach. *Adv. Sci.* **2017**, *4*, 1700194.
(20) Xiao, H.; Goddard, W. A.; Cheng, T.; Liu, Y. Cu Metal Embedded in Oxidized Matrix Catalyst to Promote CO_2 Activation and CO Dimerization for Electrochemical Reduction of CO_2. *Proc. Natl. Acad. Sci. U. S. A.* **2017**, *114*, 6685−6688.
(21) Jiang, M. P.; Huang, K. K.; Liu, J. H.; Wang, D.; Wang, Y.; Wang, X.; Li, Z. Da; Wang, X. Y.; Geng, Z.-B.; Hou, X. Y.; Feng, S. H. Magnetic-Field-Regulated TiO_2 {100} Facets: A Strategy for C-C Coupling in CO_2 Photocatalytic Conversion. *Chem.* **2020**, *6*, 2335−2346.
(22) Cheng, T.; Fortunelli, A.; Goddard, W. A. Reaction Intermediates during Operando Electrocatalysis Identified from Full Solvent Quantum Mechanics Molecular Dynamics. *Proc. Natl. Acad. Sci. U. S. A.* **2019**, *116*, 7718−7722.
(23) Sheng, H.; Oh, M. H.; Osowiecki, W. T.; Kim, W.; Alivisatos, A. P.; Frei, H. Carbon Dioxide Dimer Radical Anion as Surface Intermediate of Photoinduced CO_2 Reduction at Aqueous Cu and CdSe Nanoparticle Catalysts by Rapid-Scan FT-IR Spectroscopy. *J. Am. Chem. Soc.* **2018**, *140*, 4363−4371.
(24) Lee, S. Y.; Jung, H.; Kim, N. K.; Oh, H. S.; Min, B. K.; Hwang, Y. J. Mixed Copper States in Anodized Cu Electrocatalyst for Stable and Selective Ethylene Production from CO_2 Reduction. *J. Am. Chem. Soc.* **2018**, *140*, 8681−8689.
(25) Chou, T. C.; Chang, C. C.; Yu, H. L.; Yu, W. Y.; Dong, C. L.; Velasco-Vélez, J. J.; Chuang, C. H.; Chen, L. C.; Lee, J. F.; Chen, J. M.; Wu, H. L. Controlling the Oxidation State of the Cu Electrode and Reaction Intermediates for Electrochemical CO_2 Reduction to Ethylene. *J. Am. Chem. Soc.* **2020**, *142*, 2857−2867.
(26) Arán-Ais, R. M.; Scholten, F.; Kunze, S.; Rizo, R.; Roldan Cuenya, B. The Role of in Situ Generated Morphological Motifs and Cu(I) Species in C_{2+} Product Selectivity during CO_2 Pulsed Electroreduction. *Nat. Energy* **2020**, *5*, 317−325.
(27) Lum, Y.; Ager, J. W. Evidence for Product-Specific Active Sites on Oxide-Derived Cu Catalysts for Electrochemical CO_2 Reduction. *Nat. Catal.* **2019**, *2*, 86−93.
(28) Hohenberg, P.; Kohn, W. Inhomogeneous Electron Gas. *Phys. Rev.* **1964**, *136*, B864−B871.
(29) Kresse, G.; Hafner, J. Ab initio molecular dynamics for liquid metals. *Phys. Rev. B: Condens. Matter Mater. Phys.* **1993**, *47*, 558−561.
(30) Damia, G.; Rossanda, M. Prime Esperienze Con Fluothane in Chirurgia Generale. *Minerva Anestesiol.* **1959**, *25*, 19−25.
(31) Kresse, G.; Furthmuller, J. Efficiency of ab-initio total enery calculations for metals and semiconductors using a plane-wave basis set. *Comput. Mater. Sci.* **1996**, *6*, 15−50.
(32) Yiu, G. Rapid Communications: Antiperspirant Induced DNA Damage in Canine Cells by Comet Assay. *Toxicol. Mech. Methods* **2004**, *15*, 25−28.
(33) Lee, K.; Lundqvist, B. I. Higher-Accuracy van der Waals Density Functional. *Phys. Rev. B: Condens. Matter Mater. Phys.* **2010**, *82*, 081101.
(34) Klimeš, J.; Bowler, D. R.; Michaelides, A. Van Der Waals Density Functional Applied to Solids. *Phys. Rev. B: Condens. Matter Mater. Phys.* **2011**, *83*, 195131.
(35) Yu, X.; Zhang, X. High Coverage Water Adsorption on CuO (011) Surface. *Phys. Chem. Chem. Phys.* **2017**, *19*, 18652−18659.
(36) Sun, B. Z.; Chen, W. K.; Xu, Y. J. Reaction Mechanism of CO Oxidation on Cu_2O(111): A Density Functional Study. *J. Chem. Phys.* **2010**, *133*, 154502.
(37) Maimaiti, Y.; Nolan, M.; Elliott, S. D. Reduction Mechanisms of the CuO (111) Surface through Surface Oxygen Vancancy Formation and Hydrogen Adsorption. *Phys. Chem. Chem. Phys.* **2014**, *16*, 3036−3046.
(38) Zhang, J.; Zhang, R.; Wang, B.; Ling, L. Insight into the Adsorption and Dissociation of Water over Different CuO(111) Surfaces: The Effect of Surface Structures. *Appl. Surf. Sci.* **2016**, *364*, 758−768.
(39) Li, Q.; Fu, J.; Zhu, W.; Chen, Z.; Shen, B.; Wu, L.; Xi, Z.; Wang, T.; Lu, G.; Zhu, J. J.; Sun, S. Tuning Sn-Catalysis for Electrochemical Reduction of CO_2 to CO via the Core/Shell Cu/SnO_2 Structure. *J. Am. Chem. Soc.* **2017**, *139*, 4290−4293.
(40) Tian, Z. R.; Voigt, J. A.; Liu, J. U. N.; Mckenzie, B.; Mcdermott, M. J.; Rodriguez, M. A.; Konishi, H.; Xu, H. Complex and Oriented ZnO Nanostructures. *Nat. Mater.* **2003**, *2*, 821−826.

https://dx.doi.org/10.1021/jacs.1c00206
J. Am. Chem. Soc. 2021, 143, 2984−2993

(41) Bersani, M.; Gupta, K.; Mishra, A. K.; Lanza, R.; Taylor, S. F. R.; Islam, H.; Hollingsworth, N.; Hardacre, C.; de Leeuw, N. H.; Darr, J. A. Combined EXAFS, XRD, DRIFTS, and DFT Study of Nano Copper-Based Catalysts for CO_2 Hydrogenation. *ACS Catal.* **2016**, *6*, 5823−5833.
(42) Velu, S.; Suzuki, K.; Gopinath, C. S.; Yoshida, H.; Hattori, T. XPS, XANES and EXAFS Investigations of $CuO/ZnO/Al_2O_3/ZrO_2$ Mixed Oxide Catalysts. *Phys. Chem. Chem. Phys.* **2002**, *4*, 1990−1999.
(43) Kim, J. Y.; Rodriguez, A.; Hanson, J. C.; Frenkel, A. I.; Lee, P. L. Reduction of CuO and Cu_2O with H_2: H Embedding and Kinetic Effects in the Formation of Suboxides. *J. Am. Chem. Soc.* **2003**, *125*, 10684−10692.
(44) Zhang, W.; Huang, C.; Xiao, Q.; Yu, L.; Shuai, L.; An, P.; Zhang, J.; Qiu, M.; Ren, Z.; Yu, Y. Atypical Oxygen-Bearing Copper Boosts Ethylene Selectivity toward Electrocatalytic CO_2 Reduction. *J. Am. Chem. Soc.* **2020**, *142*, 11417−11427.
(45) Kau, L.; Spira-Solomon, D. J.; Penner-Hahn, J. E.; Hodgson, K. O.; Solomon, E. I. X-ray Absorption Edge Determination of the Oxidation State and Coordination Number of Copper: Application to the Type 3 Site in Rhus Vernicifera Lacease and Its Reaction with Oxygen. *J. Am. Chem. Soc.* **1987**, *109*, 6433−6442.
(46) Macedo, L. J. A.; Hassan, A.; Sedenho, G. C.; Crespilho, F. N. Assessing electron transfer reactions and catalysis in multicopper oxidases with operando X-ray absorption spectroscopy. *Nat. Commun.* **2020**, *11*, 316.
(47) Kattel, S.; Ramírez, P.; Chen, J.; Rodriguez, J.; Liu, P. Active Sites for CO_2 Hydrogenation to Methanol on Cu/ZnO Catalysts. *Science* **2017**, *355*, 1296−1299.
(48) Wu, J. C. S.; Huang, C. W. In Situ DRIFTS Study of Photocatalytic CO_2 Reduction under UV Irradiation. *Front. Chem. Eng. China* **2010**, *4*, 120−126.
(49) Nomura, N.; Tagawa, T.; Goto, S. In Situ FTIR Study on Hydrogenation of Carbon Dioxide over Titania-Supported Copper Catalysts. *Appl. Catal., A* **1998**, *166*, 321−326.
(50) Corson, E. R.; Kas, R.; Kostecki, R.; Urban, J.; Smith, W. A.; Mccloskey, B. D.; Kortlever, R. In Situ ATR - SEIRAS of Carbon Dioxide Reduction at a Plasmonic Silver Cathode. *J. Am. Chem. Soc.* **2020**, *142*, 11750−11762.
(51) Lee, B. J.; Kuo, M. C.; Chien, S. H. In Situ FT-IR Studies of NO Decomposition on Pt/TiO_2 Catalyst under UV Irradiation. *Res. Chem. Intermed.* **2003**, *29*, 817−826.
(52) Perez-Gallent, E.; Figueiredo, M. C.; Calle-Vallejo, F.; Koper, M. T. Spectroscopic Observation of a Hydrogenated CO Dimer Intermediate During CO Reduction on Cu(100) Electrodes. *Angew. Chem., Int. Ed.* **2017**, *56*, 3621−3624.
(53) Abdel-Mageed, A. M.; Klyushin, A.; Rezvani, A.; Knop-Gericke, A.; Schlogl, R.; Behm, R. J. Methanol Synthesis Negative Charging of Au Nanoparticles during Methanol Synthesis from CO_2/H_2 on a Au/ZnO Catalyst: Insights from Operando IR and Near-Ambient-Pressure XPS and XAS Measurements. *Angew. Chem., Int. Ed.* **2019**, *58*, 10325−10329.
(54) Kampshoff, E.; Hahn, E.; Kern, K. Correlation Betvveen Surface Stress and the Vibrational Shift of CO Chemisorbed on Cu Surfaces Elisabeth. *Phys. Rev. Lett.* **1994**, *73*, 704−707.
(55) Hollins, P.; Pritchard, J. Infrared Studies of Chemisorbed Layers on Single Crytals. *Prog. Surf. Sci.* **1985**, *19*, 275−349.
(56) Nielsen, N. D.; Smitshuysen, T. E. L.; Damsgaard, C. D.; Jensen, A. D.; Christensen, J. M. Characterization of Oxide-Supported Cu by Infrared Measurements on Adsorbed CO. *Surf. Sci.* **2021**, *703*, 121725.
(57) Sheng, H.; Zhang, H.; Song, W.; Ji, H.; Ma, W.; Chen, C.; Zhao, J. Activation of Water in Titanium Dioxide Photocatalysis by Formation of Surface Hydrogen Bonds: An In Situ IR Spectroscopy Study. *Angew. Chem., Int. Ed.* **2015**, *54*, 5905−5909.
(58) Kim, Y.; Park, S.; Shin, S.-J.; Choi, W.; Min, B. K.; Kim, H.; Kim, W.; Hwang, Y. J. Time-Resolved Observation of C−C Coupling Intermediates on Cu Electrodes for Selective Electrochemical CO_2 Reduction. *Energy Environ. Sci.* **2020**, *13*, 4301−4311.
(59) Yu, X.; Roth, J. P.; Wang, J.; Sauter, E.; Nefedov, A.; Heißler, S.; Pacchioni, G.; Wang, Y.; Wöll, C. Chemical Reactivity of Supported ZnO Clusters: Undercoordinated Zinc and Oxygen Atoms as Active Sites. *ChemPhysChem* **2020**, *21*, 2553−2564.
(60) Perez-Gallent, E.; Marcandalli, G.; Figueiredo, M. C.; Calle-Vallejo, F.; Koper, M. T. M. Structure- and Potential-Dependent Cation Effects on CO Reduction at Copper Single-Crystal Electrodes. *J. Am. Chem. Soc.* **2017**, *139*, 16412−16419.

https://dx.doi.org/10.1021/jacs.1c00206
J. Am. Chem. Soc. 2021, 143, 2984−2993